Multi-modal imaging of a single postmortem mouse brain over five orders of magnitude of resolution

Sean Foxley[1], Vandana Sampathkumar[2], Vincent De Andrade[3], Scott Trinkle[1], Anastasia Sorokina[2], Katrina Norwood[2], Patrick La Riviere[1], and Narayanan Kasthuri[2]

[1]Department of Radiology, University of Chicago, Chicago, IL, United States
[2]Department of Neurobiology, University of Chicago, Chicago, IL, United States
[3]Advanced Photon Source, Argonne National Laboratory, Lemont, IL, United States

Running Head: Multi-scale postmortem tissue imaging pipeline

Total word count: 3670

Keywords: MRI, synchrotron source x-ray tomography, electron microscopy, whole mouse brain, connectomics, multi-scale imaging

* Address correspondence to:
Sean Foxley
University of Chicago Magnetic Resonance Imaging Research Center
5841 S Maryland Ave
MC 2026
Chicago, IL 60637
Tel: 1-773-834-5119
Email: foxley@uchicago.edu

ABSTRACT

Mammalian neurons operate at length scales spanning five orders of magnitude; micron-scale-diameter myelinated axons project millimeters across brain regions, ultimately forming nanometer scale synapses on individual post-synaptic neurons. Capturing these anatomical features across that breadth of scale has required imaging samples with multiple independent imaging modalities (e.g. MRI, electron microscopy, etc.). Translating between the different modalities, however, requires imaging the *same* brain with each. Here, we imaged the same postmortem mouse brain over five orders of spatial resolution using MRI, whole brain micron-scale synchrotron x-ray tomography, and large volume automated serial electron microscopy. Using this pipeline, we can track individual myelinated axons previously relegated to axon bundles in diffusion tensor MRI or arbitrarily trace neurons and their processes brain-wide and identify individual synapses on them. This pipeline provides both an unprecedented look across a single brain's multi-scaled organization as well as a vehicle for studying the brain's multi-scale pathologies.

INTRODUCTION

The mammalian brain has the most complex cellular- and organ-wide architecture of any known biological tissue, with brains operating on multiple scales spanning orders of spatial magnitude (Lichtman & Denk, 2011). Neurons in the brain project macroscopic distances (millimeters to centimeters) (S.R., 1899), while simultaneously producing microscopic connections and plasticity-related changes between dendritic spines at the nanoscale (Grutzendler, Kasthuri, & Gan, 2002). Fully characterizing this multi-scaled architecture and the web of directional connections contained within it is decidedly nontrivial; indeed, successfully achieving such multi-scaled mapping would provide an unprecedented view into the organization of the normal central nervous system as well as a vehicle with which to study its pathologies.

No current single existing imaging modality spans the six orders of length-scale (mm to nm) required to map the whole brain while simultaneously resolving individual synapses. At macroscopic resolution scales (e.g. 0.1 to 1mm), magnetic resonance imaging (MRI) allows for both in vivo (Basser, Pajevic, Pierpaoli, Duda, & Aldroubi, 2000) and postmortem (Dyrby et al., 2007; Miller et al., 2011) mapping of neuronal tracts through a combination of diffusion-weighted imaging techniques (i.e. diffusion tensor imaging (DTI)) and post-imaging computational tractography. While powerful, these techniques cannot achieve either the micrometer-scale resolution required to observe individual neurons much less the nanometer-scale resolution required to identify individual neuronal connections. As such, MRI broadly provides brain-wide 'connectomics' of large bundles of axons (i.e. tracts) spanning macroscopic distances.

At the other end of the resolution scale, automated electron microscopy (EM) approaches provide brain sub-volume imaging at synapse-level resolution (3 nm) (Moritz Helmstaedter, 2013). These approaches remain limited by serious computational challenges, though; EM images acquired over volumes comparable to even a single voxel of MRI data (~1mm^3) is almost 2 million terabytes of data (Bouchard et al., 2016). Thus, electron microscopy, even with recent advances, is best suited for neuron 'connectomics' - reconstructing connections of individual neurons (100s of microns). Any pipeline bridging these approaches would have to solve the problems of 'context'; with such disparate resolving power, how could an EM dataset be accurately located in the context of an MRI dataset? Therefore, we had to identify an imaging technique that (a) achieved the proper micron-scale resolution throughout entire mouse brains and (b) used a sample preparation that rendered the tissue compatible with the other imaging techniques.

Synchrotron-based x-ray tomography (μCT) bridges the resolution disparity between MRI and EM; it nondestructively provides mesoscopic resolution (e.g. micron-scale) images over ~1cm^3 whole tissue volumes - the size of a small mammalian brain. Since μCT provides sub-cellular information across macroscopic distances (i.e. tracing myelinated axons in intact brains for millimeter distances), fills the resolution disparity between macroscopic (MRI) and microscopic (EM) imaging techniques (Fig. 1).

Postmortem MRI simply requires that tissue be fixed with an aldehyde, which can include those that are compatible with electron microscopy (Shepherd, Thelwall, Stanisz, & Blackband, 2009). Both whole brain synchrotron source X-ray microscopy and serial electron microscopy use osmium as the

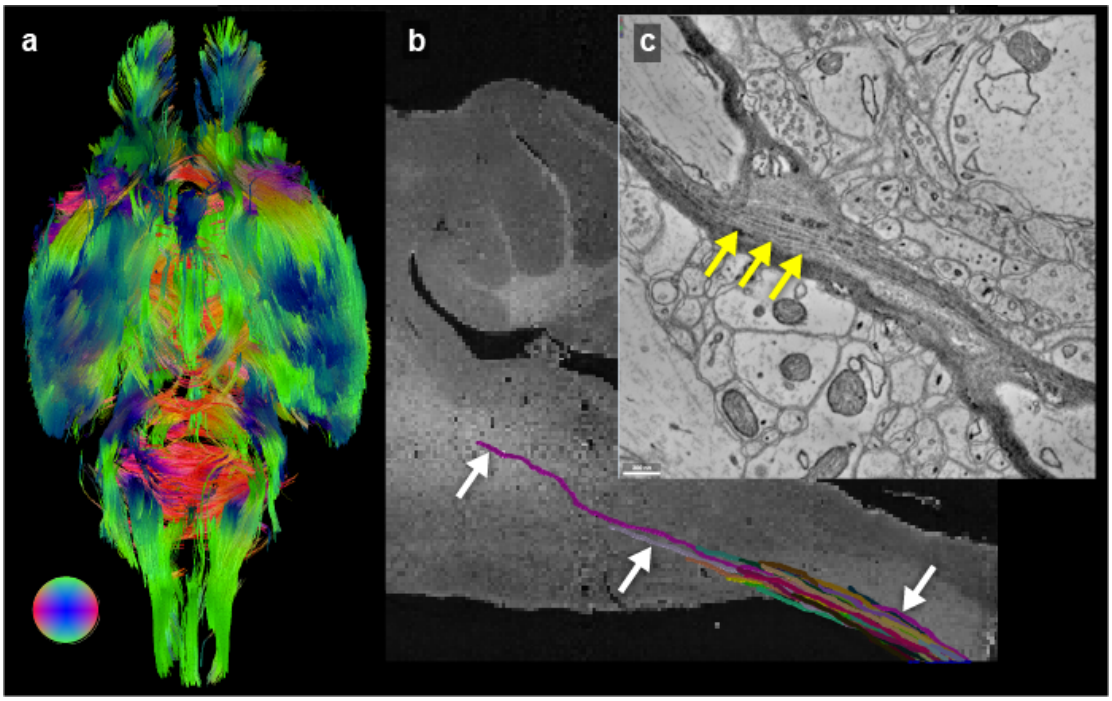

FIGURE 1 Imaging modality scale differences capture scale dependent information. By using an imaging pipeline of MRI, µCT, and EM, we can simultaneously resolve brain structures, like the white matter, at macro-, meso-, and microscopic-scales in the same brain. (a) We visualized whole brain interconnectivity by inferring white matter tracts from long scale diffusion of water along axon bundles from MRI diffusion tensor imaging. The colors denote the tract direction, as shown by the inset color sphere. (b) We can then trace individual axons (white arrows) within the same myelinated tracts over long distances with µCT, directly comparing axon paths with tracts produced in MRI. With the addition of EM, we can re-inspect the ultra-structure of individually traced axons from (b), such as (c) the individual wraps of the myelin sheath (yellow arrows). This range of scales over which we can resolve and inspects the macroscopic aspects of microscopic structures gives us an unprecedented view in to the architecture of the brain.

principle source of contrast. Therefore, µCT could remaining compatible with both MRI as well as automated EM imaging on the same sample (Dyer et al., 2017), provided that MRI is performed prior to osmium staining and tissue sectioning for EM is performed after µCT.

With µCT datasets 'bridging' MRI and EM datasets, one could simultaneously map the complete neuronal pathways from both *in vivo* and postmortem brain-wide MRI data (e.g. DTI), improve the specificity of MRI by

identifying the microstructural composition of MRI data with μCT while providing a complete rendering of the whole brain cytoarchitecture, and validate areas of interest in both MRI and μCT with subsequent nanometer reconstructions using automated serial EM. In this work we demonstrate the feasibility of such a pipeline by imaging a fixed postmortem mouse brain with MRI, preparing the whole brain for subsequent μCT and EM microscopy (Mikula, Binding, & Denk, 2012; Mikula & Denk, 2015), re-imaging the entire brain with micron resolution μCT (Dyer et al., 2017; Vescovi et al., 2018), and, finally, imaging isolated sub-volumes with automated serial EM (Kasthuri et al., 2015).

RESULTS

Whole brain imaging with μCT

Previous work has shown the compatibility of MRI and EM in postmortem tissue samples (Liu, Li, Johnson, & Wu, 2011). In order to assess the feasibility of utilizing μCT as a compatible bridge between the two, we developed a protocol for imaging entire mouse brains (1 cm^3) at micron resolution with μCT. We leveraged advances in osmium staining and embedding an entire mouse brain (Mikula et al., 2012; Mikula & Denk, 2015), tomographic imaging extending the field of view of an X-ray imaging system (Vescovi et al., 2018), and parallelization of x-ray reconstruction algorithms on national lab supercomputers (Argonne National Laboratory) for creating contiguous image stacks from the ~10 terabyte sized raw 'sinogram' data. We were able to quickly image (~8 hours) and reconstruct an entire mouse brain at 1-micron resolution (Fig. 2a). The resulting series of images formed a well-aligned isotropic dataset with sufficient resolution and contrast to capture both individual anatomic regions (Fig. 2b; the

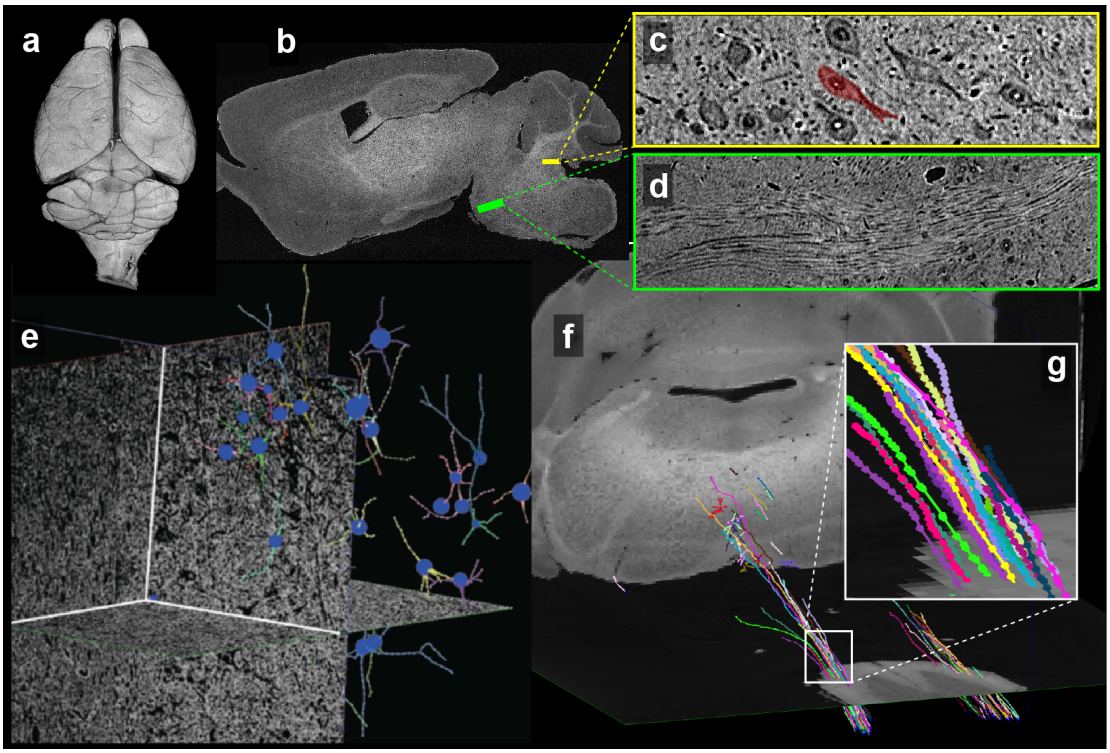

FIGURE 2 An entire mouse brain imaged at 1 micron resolution with µCT. We used high energy X-rays (23 kEV) for tomographic imaging of (a) a whole, intact mouse brain at ~1micron resolution, collecting ~10 terabytes of data in ~7 hours. A single downsampled sagittal slice (b), reveals obvious brain regions and myelinated tracts while the full resolution data contains enough detail and contrast to identify (c) individual neuronal soma, nucleus and nucleolus as well as (d) individual myelinated axons. Since µCT data are collected non-destructively, over large volumes, and with isotropic resolution, we can trace somas and their neuronal processes (dendritic trees, e) and individual myelinated axons (g) over long distances (f).

full dataset can be explored in Supplemental Movie 1) as well as underlying brain wide cytoarchitecture. For example, both neuronal somas (Fig. 2c) and long distance myelinated bundles of axons (Fig. 2d) could be clearly visualized in the same brain. Data produced sufficient detail and contrast to trace cells, their morphologies, and individual myelinated axons several millimeters (Fig. 2e-g; Supplemental Movie 2; a down-sampled version can be viewed here: https://tinyurl.com/yd9c4jdq.).

Imaging a single sample through the complete pipeline

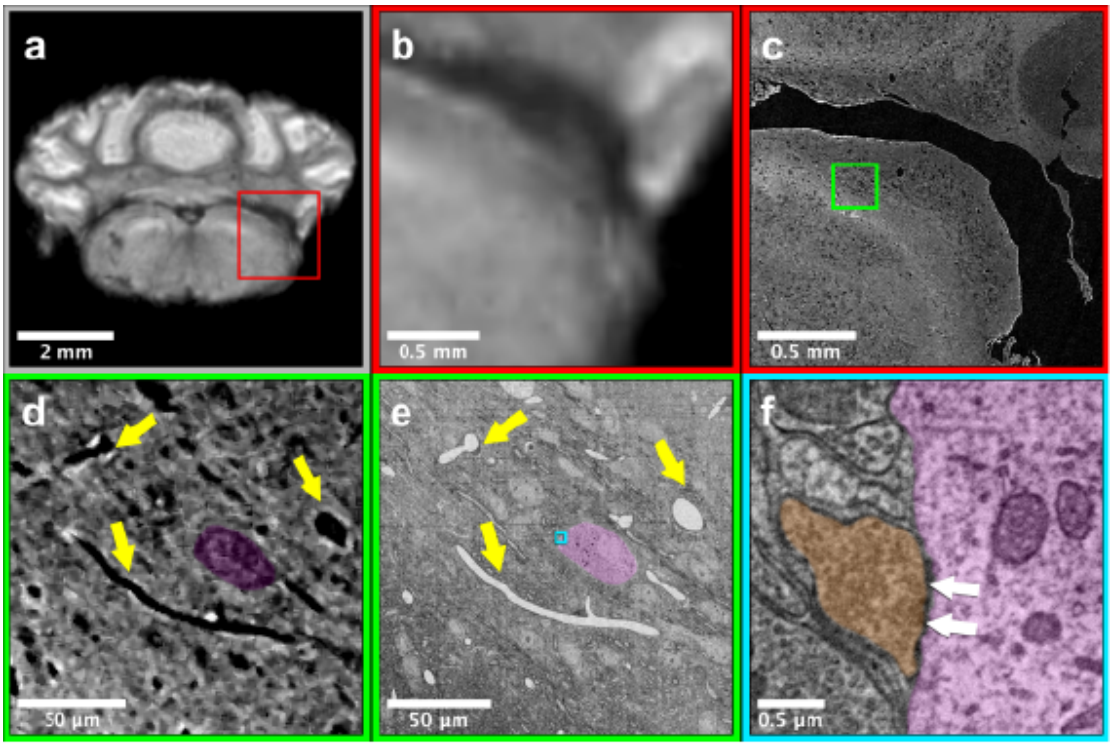

FIGURE 3 A multi-scale, multimodal pipeline for imaging the same brain from MRI to EM. The same brain was imaged using diffusion (a, b) MRI (50 micron isotropic voxels), (c, d) µCT (~ 1.2 um/voxel resolution), and (e, f) large volume serial electron microscopy (EM, ~ 3 nm/voxel resolution). (b, c) shows the same FOV from the whole brain MRI and µCT imaging, corresponding to the red ROI in (a). (d - e) show a smaller FOV in both the µCT and EM data, corresponding to the green ROI in (c). Yellow arrows indicate corresponding blood vessels, and a single neuron is labelled purple. Panel (f) highlights an individual somatic synapse (white arrows) on that soma, colored orange. The FOV of (f) is indicated by the blue ROI in (e). This pipeline demonstrates the ability to identify corresponding structures in a single brain imaged across four orders of magnitude of spatial resolution.

As the brain had been previously imaged with MRI (see below), we used the automatic tape-collecting ultra-microtome (ATUM) approach (Kasthuri et al., 2015) to collect and image 100s of ultra-thin (50nm) serial EM sections (3nm in-plane resolution) from the same region as the µCT. Thus, resolutions from each modality spanned 5 orders of magnitude on the same brain: 150µm DTI and 50µm structural MRI data, 1.2 µm µCT data, and 3 nm EM data. Typical results (Fig. 3) show similar regions from the same brain imaged with both 50µm resolution T2*-weighted structural MRI and 1.2µm resolution µCT datasets

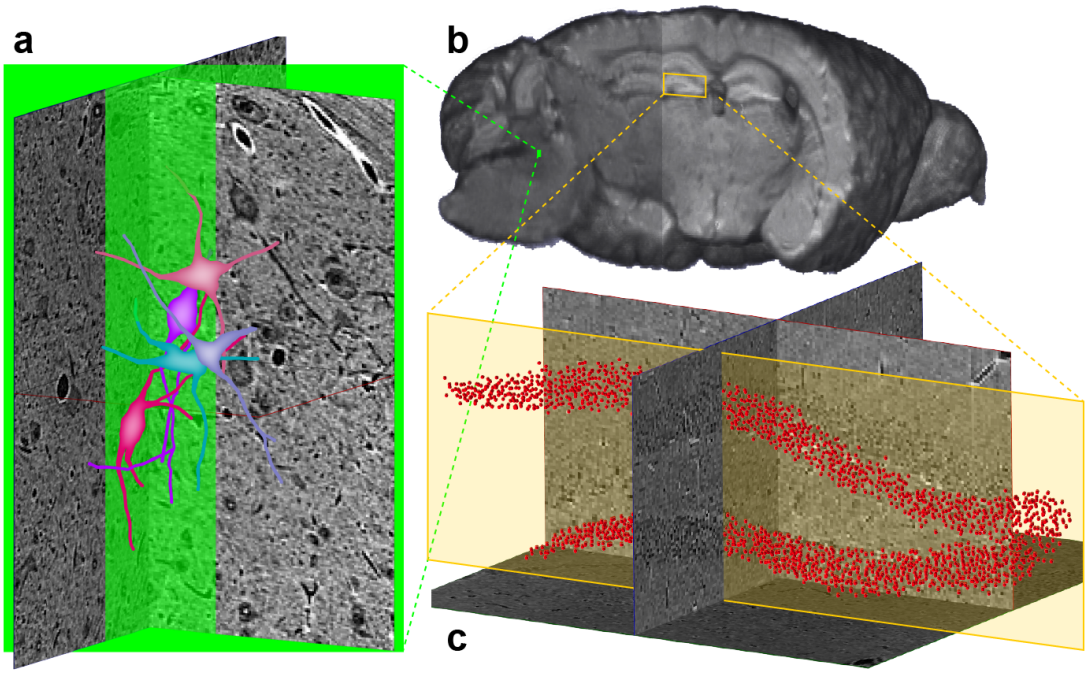

FIGURE 4 Whole brain synchrotron X-ray (μCT) provides cellular correlates of MRI contrast. (a) 3D rendering of structural MRI data used for coregistration with similar μCT data (a). Somas of the (e) medial vestibular nucleus and the (g) dentate gyrus were traced from the μCT data. While these somas are much smaller than the resolution of the MRI data, they provide possible underlying sources of contrast in the T2* weighted images

centered on a coronal slice of brainstem and cerebellum. Using vasculature and neuronal somas as fiducials to guide the subsequent EM imaging (yellow arrows, Fig. 3d-e), we found individual synapses (white arrows, Fig. 3f) on neuronal somas in the EM data. Thus we traversed from MRI data of the entire coronal cerebellum/brainstem to underlying cellular architecture of the spinal vestibular nucleus with micron-resolution μCT data and ultra-structural details of individual synapses– all from the same brain.

Comparing results of μCT with MRI

Having verified that the same tissue sample could successfully be carried through all three imaging modalities, we next explored how whole brain μCT could indicate underlying cellular correlates of MRI signals. Since both approaches produce isotropic 3D renderings of whole volumes (Figs. 2a and 4b),

this allowed for simple co-registration between the two datasets. For example, Figure 4a shows 3D somas/dendrites traced from x-ray data from the medial vestibular nucleus. While individually smaller than an MRI voxel, resolving the cytoarchitecture suggests a potential source of underlying contrast variability within an MRI dataset. Similarly, the somas in the dentate gyrus (DG) of the hippocampus are easily seen in the μCT data (Fig. 4c). Ten thousand individual cells were counted and traced within the DG over a 50μm slab of data. Again, while the individual somas are much smaller than the resolution of the MRI data, the high density of somas contribute to an anatomically dependent local variation in the MRI signal, rendering it resolvable from the surrounding structures (yellow box, Fig. 4b).

Finally, we investigated DTI, which is explicitly sensitive to underlying axon distributions. We first segmented large myelinated tracts and vasculature in the X-ray dataset using machine vision algorithms as a first pass comparison between X-ray and DTI datasets and for further fine scale analyses. For example, Figures 4a and b show linearly co-registered sagittal cross-sections of the mouse cerebellum and brain stem in both structural MRI and μCT, respectively. Overlain on the MRI structural scan are estimates of crossing fibers in each voxel. Specifically, the MRI data supported estimates of two fiber populations (Fig. 5b): one population traversing an anterior/posterior (A/P) direction and another traversing the left/right (L/R) direction (green and red cylinders, respectively). The individually traced axons from μCT were similarly color coded for comparison (Fig. 5d). The yellow boxes in Figures 5a and c indicate the location of 9 MRI voxels in which 47 individual axons (27 L/R, 20 A/P) were traced in the x-ray data. Figure 5a shows the MRI diffusion direction estimates overlain on top

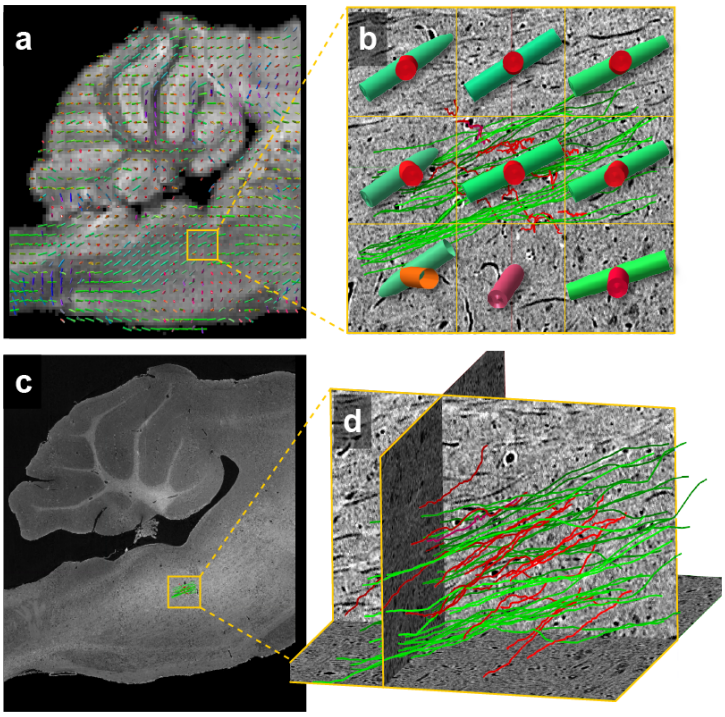

FIGURE 5 Whole brain synchrotron X-ray (µCT) provides axpnal correlates of MRI contrast) DTI data of the same brain were also acquired. A shown are automated segmentations of long distance myelinated tracts (green) and large vasculature (red) from the uCtr data. B shows the DTI for the MRI. Using this dat t we identify zoome dup versions. Principal and secondary fiber population estimates are shown overlaid on a sagittal slice of a corresponding structural MRI scan (green indicates fiber orientation along the rostral/caudal axis, red indicates left/right) as well as in (i) the magnified 9 voxels. (j) The mCT data from the same brain has been linearly registered to the MRI structural data and (k) individually traced axons from the mCT data are shown with the same color scheme as (h). Both principal and secondary fiber estimates from DTI data indicate quite similar orientations as the underlying population of individual axons traced from the mCT data, as seen by (i) the agreement of the DTI direction estimates superimposed on the individual traced individual axons.

of the axons. The populations of axons traced in the x-ray data clearly follow similar directions to the MRI diffusion direction estimates while negligible numbers of axons in the x-ray data traverse directions other than two estimated with the DTI analyses. This supports the accuracy of the MRI diffusion model used to estimate directions of underlying fiber populations.

DISCUSSION

We describe a pipeline using three imaging modalities, providing unprecedented views across orders of magnitude of a single mouse brain sample. Whole brain imaging from the meso- to the nano-scale will allow for potentially novel understandings and/or interpretations of results within each modality, currently constrained by scale-dependent differences in each individual approach. For example, for tract tracing, MRI data will provide low-resolution, whole-brain estimates of neural tracts (Fig. 1a), μCT will provide long range trajectories of individual myelinated axons in those tracts (Fig. 1b), validating and extending the MRI data, and the EM would provide reconstructions of individual wrappings of myelin sheaths (Fig. 1c) or the eventual synaptic targets of those same myelinated axons.

Other whole brain imaging approaches often rely on genetic expression of fluorescent proteins to both label a subset (often < 1%) of neurons and to target labeling of neurons deep in the brain. Genetic expression limits these approaches to a small range of tractable animals (i.e. mouse, fly, and worm (Kwanghun Chung & Karl Deisseroth, 2013)). Subset labeling, by necessity, precludes detailing how different brain structures, like neuronal somas, vasculature, or myelinated tracts, relate to each other. Finally, whole brain optical approaches, whether based on expansion (Chen, Tillberg, & Boyden, 2015) or optical index matching (K. Chung & K. Deisseroth, 2013), often remove cell membranes, making them essentially incompatible with subsequent large volume electron microscopy.

Because of the contrast mechanisms of each imaging modality, this pipeline works on brains (or any other organ type) of any species. MRI contrast is explicitly sensitive to tissue water, regardless of tissue type. Further, osmium

is used as a contrast stain for both μCT and EM because it stains membranes of any type of cell in any type of tissue (Palay, Mc, Gordon, & Grillo, 1962). Therefore, in a single brain sample, our pipeline reveals the relative locations of nearly every soma, blood vessel, myelinated axon and synapse.

Clear advantages of using whole brain μCT as an intermediate approach is that datasets are: (1) isotropic resolution, facilitating tracing in any direction, (2) imaged through intact brains with minimal deformation, obviating computationally difficult large scale alignments (Kwanghun Chung & Karl Deisseroth, 2013; Saalfeld, Fetter, Cardona, & Tomancak, 2012), and (3) compatible with sample preparation for downstream electron microscopy.

As the 'normal' cytoarchitecture of different structures within the brain are characterized with the μCT and EM data, we can begin to more comprehensively understand the contributions of the various cellular components to the measured MRI signal. This is particularly useful in studying pathologies of the brain. Pathological alterations in neural function and behavior are well documented, but our understanding of their cellular underpinnings remains fragmentary. The complexity of brain circuitry and the marked heterogeneity of neuronal sizes and shapes across brains can mask even dramatic changes in specific neuronal subsets, making structural analyses difficult. Using μCT and EM to inform contrast variability in MRI data over entire brains would significantly narrow the search for pathological structural change and lead improved specificity in MRI. This would also lead to potential *in vivo* MRI biomarkers of disease. The next generation of synchrotrons currently under construction (Schmidt et al., 2018) should allow for even deeper penetration of samples with the possibility of imaging even larger brains in their entirety.

Finally, by instantiating our imaging pipeline in a national laboratory, we provide a path for access for future investigations by other researchers at a no-cost facility open to researchers worldwide.

MATERIALS AND METHODS

Sample preparation

All procedures performed on animals followed protocols approved by the Institutional Animal Care and Use Committee and were in compliance with the Animal Welfare Act and the NIH Guide for the Care and Use of Laboratory Animals. An eight week old, female C57bl6 mouse was deeply anesthetized with 60 mg/kg pentobarbital. The mouse was transcardially perfused with a solution (pH 7.4) of 0.1M Sodium Cacodylate and heparin (15 units/ml) immediately followed by a solution of 2% paraformaldehyde, 2.5% glutaraldehyde, and 0.1M Sodium Cacodylate (pH 7.4). The brain was carefully removed from the skull and post-fixed in the same fixative for 48h at 4°C. The order of serial imaging was magnetic resonance imaging (MRI), synchrotron-based x-ray tomography (μCT), and then electron microscopy (EM).

MRI

The resected and aldehyde fixed brain was washed in PBS for 72h to remove fixative, which can be deleterious to MRI imaging (Dyrby et al., 2007; Shepherd et al., 2009). Just prior to MR imaging, brains were dried of excess PBS and placed in 10 ml falcon tubes. Tubes were filled with Fluorinert (FC-3283, 3M Electronics) for susceptibility matching and to improve shimming.

μCT

After MRI imaging the whole brain was transferred to 0.1M cacodylate buffer. Whole brain staining with osmium and other heavy metals and whole brain dehydration and plastic embedding were done as described (Mikula et al., 2012; Mikula & Denk, 2015). The brain was stained with multiple rounds of osmium and reduced osmium followed by dehydration and plastic embedding (Mikula & Denk, 2015).

Electron Microscopy

After μCT imaging, the brain block was removed from the rotation stage and hundreds of serial ultra-thin sections (1mm x 1mm x 50nm) were collected on tape and imaged inside a scanning electron microscope (Kasthuri et al., 2015).

Acquisition protocols

MRI

Data were acquired at 9.4 Tesla (20 cm internal diameter, horizontal bore, Bruker BioSpec Small Animal MR System, Bruker Biospin, Billerica, MA) using a 6cm high performance gradient insert (maximum gradient strength: 1000 mT/m, Bruker Biospin) and a 35mm internal diameter quadrature volume coil (Rapid MR International, Columbus, Ohio). The brain was aligned such that the anterior/posterior portion of the olfactory limb of the anterior commissure (AC) was approximately parallel to the magnetic field of the scanner and the hemispheric midline was parallel to the scanner YZ plane.

Third order shimming was iteratively performed over an ellipse that encompassed the entire brain, but did not extend beyond the boundaries of the falcon tube/Fluorinert interface, using the Paravision mapshim protocol. B0 maps were produced by recording the voxel-wise frequency of the peak of the resonance, including additional sub-spectral resolution frequency produced by

estimating the maximum peak amplitude of the resonance, described below. This was consistent with previously reported work (Foxley, Domowicz, Karczmar, & Schwartz, 2015; Foxley, Karczmar, & Takahashi, 2018), which described a high degree of field homogeneity across samples.

DTI was performed using a standard diffusion-weighted 3D spin echo sequence (TR = 400ms, TE = 18.5ms, b value = 3000 s/mm^2, d = 5ms, D = 11.04ms, spatial resolution = 150um isotropic, number of b0's = 16, number of non-collinear directions = 30, receiver bandwidth = 200kHz, partial Fourier along first phase encoding direction = 7/8, duration = 55hrs 19min 40sec).

Structural MRI data were acquired using a multi-echo gradient echo sequence. This produces a 4D dataset, where data are sampled along time in each spatial voxel to acquire the free induction decay (FID). Sequence parameters were chosen so that the entire voxel-wise FID was sampled to the noise floor (TR = 1000 ms, TE of first echo = 2.74ms, echo spacing = 2.74ms, number of echoes = 192, receiver bandwidth = 75kHz, flip angle = 68°, 100mm isotropic resolution, 4 averages, duration = 12 hours).

μCT

The microCT data were acquired at the 32-ID beamline at the Advanced Photon Source, Argonne National Laboratory. The setup consists of a 1.8 cm-period undulator operated at a low deflection parameter value of K = 0.26. This yields a single quasi-monochomatic peak of energy 25 keV without the losses incurred by use of a crystal monochromator. For a sample 68 m from the undulator, this produces a photon fluence rate of about 1.8 x 10^7 photons s^{-1} μm^{-2}.

The x-rays were imaged by using a 10 μm thick thin-film LuAG:Ce scintillator to convert the x-ray intensity pattern into a visible-light image, which was then

magnified using a 5X long Mitutoyo long working distance microscope objective onto a visible-light 1920 X 1200 pixel CMOS camera (Point Gray GS3-U3-51S5M-C). The effective object space pixel size is 1.17 μm and the field of view 2.25 x 1.41 mm^2. The thickness of the thin-film scintillator matches the depth of focus of the objective lens in order to achieve a spatial resolution equivalent to the resolving power of the lens (1.3 μm for a NA of 0.21). Since the camera field of view (FOV) is substantially smaller than the mouse brain, we employed a mosaic strategy (Vescovi et al., 2018).

The sample was mounted on an air-bearing rotary stage (PI-Micos UPR-160 AIR) with motorized *x–y* translation stages located underneath and *x–y* piezo stages on top. Typical exposure times for a single projection image at one mosaic grid point and one rotation angle were 30 ms, and 3600 rotation angles were used at each grid point. The sample was translated through a 6 x18 tomosaic grid.

Electron microscopy

After completion of μCT, a region of interest (ROI) was identified in the brainstem and cerebellum. The block was trimmed to the ROI and 50nm thick serial sections were collected on aluminium tape and attached to a wafer (Kasthuri et al., 2015). The ultrathin sections were imaged with an in lens T1 detector on Apreo SEM (ThermoFisher Scientific). Low-resolution images were obtained with 135nm in-plane resolution. High-resolution images were obtained with 3nm in-plane resolution. Images were collected with a 3μs dwell time.

Data processing and analysis

MRI

Data were reconstructed, processed, and analyzed with IDL 8.2 (ITT Visual Information Solutions, Boulder CO), Matlab 2014b (The MathWorks Inc., Natick, MA, 2012), and FSL 5.0.9 (FMRIB Software Library, FMRIB, Oxford, UK).

3D multiple-gradient echo data were reconstructed to produce voxel-wise water spectra. Each complex 4D dataset ($x \times y \times z \times t$) was Fourier transformed along time to produce three spatial dimensions and one spectral dimension ($x \times y \times z \times u$). A T2* weighted structural image was constructed from the spectral data, where image contrast was produced by isolating the maximum voxel-wise signal amplitude of the water spectrum (Al-Hallaq et al., 2002). This was achieved by identifying and storing the voxel-wise maximum peak signal amplitude in a 3D array with the same spatial dimensions as the acquisition.

The mean b = 0 s/mm^2 dataset from the diffusion acquisition was registered to the respective structural image via affine transformation using the FSL linear registration tool (FLIRT) (Jenkinson & Smith, 2001). Subsequent diffusion data were identically registered using the resultant transformation matrix. Principal, secondary, and tertiary diffusion directions were estimated using BEDPOSTX (Behrens et al., 2003).

μCT

Following the tomosaic pipeline, the acquired sub-sinograms were registered with sub-pixel shifting and stitched through pyramid blending into a complete sinogram. The center of rotation of the composite sinogram was estimated using an entropy-based approach. Reconstruction of the entire dataset in whole-block mode is performed using the gridrec implementation of direct Fourier reconstruction implemented in the TomoPy package. The reconstructed image volume was 11.7 x 11.7 x 17.7 mm^3 with 1.17 μm isotropic voxels. To minimize

storage and memory requirements, the reconstructed image volume was trimmed to the smallest volume containing the entire brain and stored in 8-bit format (the camera acquires 11-bit data and 32-bit floats were used during reconstruction processing).

Following reconstruction, μCT data were visualized using Neuroglancer (https://github.com/google/neuroglancer), a high-performance WebGL based viewer for large volumetric datasets. Neuroglancer allows for memory-efficient loading of cross-sectional displays across arbitrary planes in the data. This allowed for simple, fine-tuned manual localization of the visible structures in the EM sections within the μCT dataset, using large blood vessels and neuronal somas as landmarks. Our μCT data can be publicly viewed online through Neuroglancer (http://neuroglancer-demo.appspot.com/) using http://nova.kasthurilab.com:8000/neuroglancer/recon_crop8_neurog/image as the precomputed source link.

All manually labeling of somas and myelinated axons was performed using Knossos (M. Helmstaedter, Briggman, & Denk, 2011).

ACKNOWLEDGEMENTS

The authors thank Shawn Mikula for help with sample preparation for μCT and EM. S.F would like to thank the MRIS and MRIRC. N.K. and V.S. are supported from a Technical Innovation Award from the McKnight foundation, a Brain Initiative of the National Institutes of Health (U01 MH109100), and National Science Foundation Neuro Nex grant. P.LR. is partially supported by the National Institutes of Health (R01EB026300). S.T. is supported by the National Institute of Neurological Disorders and Stroke of the National Institutes of Health

(F31NS113571). Additional funding supporting this work was provided by the National Institutes of Health (S10-OD025081, S10-RR021039, and P30-CA14599). This research used resources of the Advanced Photon Source, a U.S. Department of Energy (DOE) Office of Science User Facility operated for the DOE Office of Science by Argonne National Laboratory under Contract No. DE-AC02-06CH11357. This research also used resources of the Argonne Leadership Computing Facility, which is a DOE Office of Science User Facility supported under Contract DE-AC02-06CH11357. Finally, the authors would like to thank Viren Jain and Jennifer Neely for thoughtful comments and discussions over the course of the preparation of the manuscript.

ABBREVIATIONS

MRI – Magnetic Resonance Imaging

DTI – Diffusion tensor Imaging

EM - Automated Electron Microscopy

μCT - Synchrotron-based x-ray tomography

AUTHOR CONTRIBUTIONS

S.F., P.LR., and N.K. conceived and designed the imaging pipeline. S.F. acquired and processed MRI data. V.DA. designed the μ-CT system used for data collection and contributed in reconstruction of μ-CT data. V.S. collected all EM data. S.T. registered MRI, μCT, and EM data. S.F., A.S., and K.N. traced/segmented μCT data and S.F. registered results to MRI data. S.F. and N.K. wrote the final manuscript and all authors contributed to its revision.

COMPETING INTERESTS

The authors declare no competing or conflicts of interest.

REFERENCES

Al-Hallaq, H. A., Fan, X., Zamora, M., River, J. N., Moulder, J. E., & Karczmar, G. S. (2002). Spectrally inhomogeneous BOLD contrast changes detected in rodent tumors with high spectral and spatial resolution MRI. *NMR in biomedicine, 15*(1), 28-36.

Basser, P. J., Pajevic, S., Pierpaoli, C., Duda, J., & Aldroubi, A. J. M. r. i. m. (2000). In vivo fiber tractography using DT‐MRI data. *Magnetic resonance in medicine, 44*(4), 625-632.

Behrens, T. E., Woolrich, M. W., Jenkinson, M., Johansen-Berg, H., Nunes, R. G., Clare, S., et al. (2003). Characterization and propagation of uncertainty in diffusion-weighted MR imaging. [Research Support, Non-U.S. Gov't]. *Magn Reson Med, 50*(5), 1077-1088.

Bouchard, K. E., Aimone, J. B., Chun, M., Dean, T., Denker, M., Diesmann, M., et al. (2016). High-performance computing in neuroscience for data-driven discovery, integration, and dissemination. *Neuron, 92*(3), 628-631.

Chen, F., Tillberg, P. W., & Boyden, E. S. (2015). Expansion microscopy. *Science*, 1260088.

Chung, K., & Deisseroth, K. (2013). CLARITY for mapping the nervous system. *Nat Methods, 10*(6), 508-513.

Chung, K., & Deisseroth, K. (2013). CLARITY for mapping the nervous system. *Nature methods, 10*(6), 508.

Dyer, E. L., Gray Roncal, W., Prasad, J. A., Fernandes, H. L., Gursoy, D., De Andrade, V., et al. (2017). Quantifying Mesoscale Neuroanatomy Using X-Ray Microtomography. *eNeuro, 4*(5).

Dyrby, T. B., Søgaard, L. V., Parker, G. J., Alexander, D. C., Lind, N. M., Baaré, W. F., et al. (2007). Validation of in vitro probabilistic tractography. *Neuroimage, 37*(4), 1267-1277.

Foxley, S., Domowicz, M., Karczmar, G. S., & Schwartz, N. (2015). 3D high spectral and spatial resolution imaging of ex vivo mouse brain. [Research Support, American Recovery and Reinvestment Act

Research Support, N.I.H., Extramural]. *Med Phys, 42*(3), 1463-1472.

Foxley, S., Karczmar, G. S., & Takahashi, K. (2018). The effects of variations in tissue microstructure from postmortem rat brain on the asymmetry of the water proton resonance. *Magn Reson Med*.

Grutzendler, J., Kasthuri, N., & Gan, W. B. (2002). Long-term dendritic spine stability in the adult cortex. *Nature, 420*(6917), 812-816.

Helmstaedter, M. (2013). Cellular-resolution connectomics: challenges of dense neural circuit reconstruction. *Nature methods, 10*(6), 501.

Helmstaedter, M., Briggman, K. L., & Denk, W. (2011). High-accuracy neurite reconstruction for high-throughput neuroanatomy. *Nat Neurosci, 14*(8), 1081-1088.

Jenkinson, M., & Smith, S. (2001). A global optimisation method for robust affine registration of brain images. [Comparative Study
Research Support, Non-U.S. Gov't]. *Med Image Anal, 5*(2), 143-156.
Kasthuri, N., Hayworth, K. J., Berger, D. R., Schalek, R. L., Conchello, J. A., Knowles-Barley, S., et al. (2015). Saturated Reconstruction of a Volume of Neocortex. *Cell, 162*(3), 648-661.
Lichtman, J. W., & Denk, W. (2011). The big and the small: challenges of imaging the brain's circuits. *Science, 334*(6056), 618-623.
Liu, C., Li, W., Johnson, G. A., & Wu, B. (2011). High-field (9.4 T) MRI of brain dysmyelination by quantitative mapping of magnetic susceptibility. *Neuroimage, 56*(3), 930-938.
Mikula, S., Binding, J., & Denk, W. (2012). Staining and embedding the whole mouse brain for electron microscopy. *Nat Methods, 9*(12), 1198-1201.
Mikula, S., & Denk, W. (2015). High-resolution whole-brain staining for electron microscopic circuit reconstruction. *Nat Methods, 12*(6), 541-546.
Miller, K. L., Stagg, C. J., Douaud, G., Jbabdi, S., Smith, S. M., Behrens, T. E., et al. (2011). Diffusion imaging of whole, post-mortem human brains on a clinical MRI scanner. *Neuroimage, 57*(1), 167-181.
Palay, S. L., Mc, G.-R. S., Gordon, S., Jr., & Grillo, M. A. (1962). Fixation of neural tissues for electron microscopy by perfusion with solutions of osmium tetroxide. *J Cell Biol, 12*, 385-410.
S.R., C. (1899). *Textura del sistema nervioso del hombre y de los vertebrados* (Vol. 1). Madrid.: Imprenta y Librería de Nicolás Moya
Saalfeld, S., Fetter, R., Cardona, A., & Tomancak, P. (2012). Elastic volume reconstruction from series of ultra-thin microscopy sections. *Nature methods, 9*(7), 717-720.
Schmidt, O., Benda, E., Capatina, D., Clute, T., Collins, J., Erdmann, M., et al. (2018). *Beamline Engineering Overview for the APS Upgrade.* Paper presented at the MEDSI, Paris, France.
Shepherd, T. M., Thelwall, P. E., Stanisz, G. J., & Blackband, S. J. (2009). Aldehyde fixative solutions alter the water relaxation and diffusion properties of nervous tissue. *Magn Reson Med, 62*(1), 26-34.
Vescovi, R., Du, M., de Andrade, V., Scullin, W., Gursoy, D., & Jacobsen, C. (2018). Tomosaic: efficient acquisition and reconstruction of teravoxel tomography data using limited-size synchrotron X-ray beams. *J Synchrotron Radiat, 25*(Pt 5), 1478-1489.